



**HAL**  
open science

# Numerical study of friction-induced instability and acoustic radiation - Effect of ramp loading on the squeal propensity for a simplified brake model

Kevin Soobbarayen, Jean-Jacques Sinou, Sébastien Besset

## ► To cite this version:

Kevin Soobbarayen, Jean-Jacques Sinou, Sébastien Besset. Numerical study of friction-induced instability and acoustic radiation - Effect of ramp loading on the squeal propensity for a simplified brake model. *Journal of Sound and Vibration*, 2014, 333 (21), pp.5475-5493. 10.1016/j.jsv.2014.05.037 . hal-01009250

**HAL Id: hal-01009250**

**<https://hal.science/hal-01009250>**

Submitted on 17 Jun 2014

**HAL** is a multi-disciplinary open access archive for the deposit and dissemination of scientific research documents, whether they are published or not. The documents may come from teaching and research institutions in France or abroad, or from public or private research centers.

L'archive ouverte pluridisciplinaire **HAL**, est destinée au dépôt et à la diffusion de documents scientifiques de niveau recherche, publiés ou non, émanant des établissements d'enseignement et de recherche français ou étrangers, des laboratoires publics ou privés.

# Numerical study of friction-induced instability and acoustic radiation - Effect of ramp loading on the squeal propensity for a simplified brake model

K. Soobbarayen<sup>1,a</sup>, J.-J. Sinou<sup>1,b</sup>, and S. Besset<sup>1,c</sup>

<sup>1</sup>*Laboratoire de Tribologie et Dynamique des Systèmes, UMR CNRS 5513,  
Ecole Centrale de Lyon, 36 avenue Guy de Collongue 69134 Ecully Cedex, France*  
{<sup>a</sup>kevin.soobbarayen, <sup>b</sup>jean-jacques.sinou, <sup>c</sup>sebastien.besset}@ec-lyon.fr

## Abstract

This paper presents a numerical study of the influence of loading conditions on the vibrational and acoustic responses of a disc brake system subjected to squeal. A simplified model composed of a circular disc and a pad is proposed. Nonlinear effects of contact and friction over the frictional interface are modelled with a cubic law and a classical Coulomb's law with a constant friction coefficient. The stability analysis of this system shows the presence of two instabilities with one and two unstable modes that lead to friction-induced nonlinear vibrations and squeal noise. Nonlinear time analysis by temporal integration is conducted for two cases of loadings and initial conditions: a static load near the associated sliding equilibrium and a slow and a fast ramp loading. The analysis of the time responses show that a sufficiently fast ramp loading can destabilize a stable configuration and generate nonlinear vibrations. Moreover, the fast ramp loading applied for the two unstable cases generates higher amplitudes of velocity than for the static load cases. The frequency analysis shows that the fast ramp loading generates a more complex spectrum than for the static load with the appearance of new resonance peaks. The acoustic responses for these cases are estimated by applying the multi-frequency acoustic calculation method based on the Fourier series decomposition of the velocity and the Boundary Element Method. Squeal noise emissions for the fast ramp loading present lower or higher levels than for the static load due to the different amplitudes of velocities. Moreover, the directivity is more complex for the fast ramp loading due to the appearance of new harmonic components in the velocity spectrum. Finally, the sound pressure convergence study shows that only the first harmonic components are sufficient to well describe the acoustic response.

## 1 Introduction

Brake squeal is characterized by noise emissions in the frequency range [1; 20] kHz. It mainly appears for structures presenting nonlinear effects and non-conservative forces such as the friction forces, over a frictional interface [1]. During the braking process of a disc brake system, a hydraulic pressure is applied over the back-plate of the pad. Then, the pad makes contact with the rotating disc and the system reaches a quasi-static sliding equilibrium configuration. This sliding equilibrium can be unstable due to friction and a slight disturbance gives rise to the divergence from this equilibrium. Finally, nonlinear effects generate nonlinear vibrations giving rise to noise emissions called squeal noise. Noise pollution is a major concern in industry due to expensive warranty costs and the necessity to constantly improve the vehicles acoustic convenience. Several mechanisms of initiation acting at different scales associated with contact, friction or chaos [2] have been identified but squeal comprehension is still not complete.

One of the most important point in the numerical study of squeal is the interface modelling. Actually the nonlinear laws which represent the contact and friction play a capital role in squeal initiation and an extensive review of the classical formulations can be found in [3, 4]. Involving the contact phenomena, two main formulations can be used and as explained in [5] the most realistic is the penalty contact law which avoid the penetration between the disc and the pad. In this paper the author highlights the influence of the contact tribology on brake squeal and shows that contact and interface topology are essential in squeal initiation. However, the main numerical limitation in avoiding penetration is that the time computation of the dynamic response can be prohibitive. Another way to model contact is to use smooth contact by introducing contact elements over the frictional interface. This phenomenological method allows us to reduce computation time and is easy to implemented. Moreover, even if it allows penetration between the two substructures, it is able to capture some squeal instabilities [6]. The main limitations are the contact stiffnesses determination and a less realistic dynamic response. However, it is well adapted to simplify phenomenological model and this simplified contact law will be used in the present paper. On the other hand, the Coulomb's friction law is commonly used and the key point is the friction coefficient function. It has been shown by Butlin et al. [7] that a sliding velocity dependent friction coefficient is essential to be in agreement with experiments: this is the most realistic way to model the friction forces. It is also possible to use a constant friction coefficient but the main issue is the fact that all the instabilities cannot be represented as the stick-slip motion. However, the mode-coupling instabilities can be well represented by this simple formulation and, as for the smooth contact law, are appropriated for phenomenological study involving mode-coupling.

The calculation of the dynamic and acoustic responses associated with squeal occurrences is a complex task which is mainly composed of three steps. First of all, the detection of the instabilities and the squeal occurrences prediction are conducted with a stability analysis. This analysis is based on a complex eigenvalues analysis and allows us to detect the squeal frequencies. In [8], Ouyang explains that this analysis provides all unstable eigenvalues in one run and so it allows us to detect when an unstable motion and a potential squeal noise may occur. Therefore, parametric investigation of the stability can be performed with respect to several parameters as the friction coefficient, the contact parameters... In [9], Fritz et al. focus on the stability for a finite element model of an automotive disc brake. The authors show that the modal damping parameters can change the mode-coupling patterns. Those results are in good agreement with the results of Hoffmann et al. [10] who show the influence of the damping parameters on the mode coupling of a minimal model with two degrees of freedom. Moreover, Massi et al. [11] show that squeal occurrence predictions are in good agreement with the experiments for an automotive disc brake system. Chevillot et al. [12] provide simulations and experiments of a nonlinear aircraft braking system and show that the stability of the numerical model is efficient to experimentally reproduce squeal instability. For the parameters corresponding to potential squeal, the next step corresponds to nonlinear time analysis that is conducted to calculate the friction-induced vibrations [13]. Finally, the acoustic response is estimated with the multi-frequency acoustic calculation method as explained in [14].

However, it is now recognized that, in some cases, the stability analysis is not sufficient to allow comparison between numerical simulations and experiments. Actually, if the nonlinear time analysis does not satisfy the stability analysis assumptions, then the squeal motion cannot be well predicted. For example, the temporal integration has to be initialized near the sliding equilibrium configuration to be close to the associated linear system. As mentioned in [15], the complex eigenvalues analysis may lead to an underestimation or an over-estimation of the "unstable modes" observed during the transient and stationary self-excited vibrations. It appears that different nonlinear behaviours can be obtained for the same friction coefficient by only

introducing a different initial disturbance around the nonlinear equilibrium point. The nonlinear time analysis shows that the displacement profile is modified and the spectrum analysis highlights the appearance of new harmonic components. This fact was also illustrated in [13]: the authors propose a global strategy based on experiments and transient simulations for squeal understanding and characterization on industrial railway brakes. This study showed that the nonlinear transient vibrations may induce the appearance of new resonance peaks and so that the stability is not sufficient to predict squeal noise. Another limitation of the stability analysis is that it does not consider time dependent loading but only static load. Therefore, this analysis does not allow the detection of squeal associated with a real braking force profile. In the present paper, this will be investigated by conducting temporal integration as mentioned in [16].

Despite great insights in the understanding and modelling of brake squeal, only few numerical studies propose a complete characterization of squeal with the calculation of the nonlinear vibrations and the estimation of the noise emissions. In [17], von Wagner et al. investigate the stability analysis of a finite element model of a disc brake, with respect to the friction coefficient. A transient analysis is performed and the self-excited vibrations are calculated near the sliding equilibrium. This numerical approach allows for choosing the model parameters to perform experimental test. The author is able of reproducing squeal in laboratory and provides an experimental estimation of squeal noise which reaches 82 dB. Another relevant work carried out by Lee and Singh [18] proposes to calculate the sound pressure for a simplified disc brake rotor subjected to modal force vibrations with a semi-analytical model. The results have been validated by the Boundary Element Method and experiments. More recently, Oberst et al. [19] provide an extensive numerical study of the influence of pad geometry on the acoustic radiations and highlight the necessity to use a realistic representation of the frictional interface. A precise study of the influence of pad chamfers and disc-pad lift-offs on the directivity patterns has been performed and the authors show that these considerations strongly modify the noise levels and the directivity. A peculiar horn effect which generates a noise level increase has also been numerically observed due to the presence of chamfers. Moreover, one of the conclusions is that the interface dynamics (i.e. the contact/friction formulations and the interface mesh refinement) has a strong impact on the acoustic behaviour. For the two previously mentioned papers, the dynamic response has been generated with a directly calculated forced response. This allows us to estimate the noise radiation for a given frequency and thus, to investigate the influence of parameters on several harmonic components which contribute to squeal noise. In the present work, the acoustic study will aim at estimating the global noise radiation associated with a “non-forced” dynamic response (the nonlinear dynamic response is only generated by an initially unstable equilibrium point, i.e. friction-induced vibrations) with a complete frequency spectrum.

In the present paper, a particular attention is drawn to the influence of time dependent loading on the dynamic response and the acoustic radiations for a brake system subjected to mode-coupling instabilities. The two main questions of interest are: (1) can the loading profile contribute to squeal initiation? (2) How the loading profile modifies the nonlinear dynamics and the acoustics of a system subjected to nonlinear friction-induced vibrations?

To achieve the previous objectives, the paper is organized as follows: firstly, the disc brake model and the loading conditions are presented. Then, the Boundary Element Method and the treatment of the normal velocity used in the acoustic study are detailed. Secondly, numerical simulations of brake squeal that are conducted by: performing a stability analysis with respect to the friction coefficient, calculating the dynamic responses associated with static load for classical cases of instabilities (i.e. a stable case and two cases presenting one and two unstable modes), calculating for the same cases the dynamic responses for ramp loadings with different growth rates. The influence of the ramp loading is investigated by comparing both dynamic

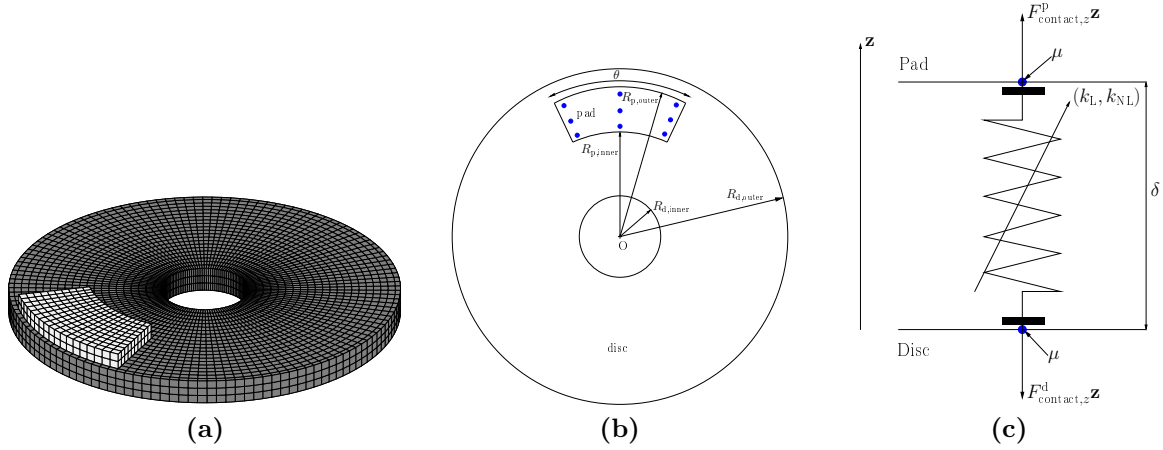


**Fig. 1.** Brake system model and contact model. (a): simplified brake system; (b): position of the pad, contact nodes (•) and geometrical parameters; and (c): nonlinear contact elements over the interface.

responses and frequency spectrum. Finally, the impact of this time dependent loading on the associated noise emission is investigated: the multi-frequency acoustic calculation method is first remembered, then all the acoustic radiations of the previous cases are calculated and compared to investigate the influence of the ramp loading on the squeal noise.

## 2 Brake system model

Most disc brake systems are composed of a disc, a calliper which contains pads, a wheelhouse and the geometry of this kind of system can be complex. However, the two main components involved in squeal phenomenon are the disc and the pad which share a friction interface. In this paper, a simplified brake system model is studied and it is composed of a disc and a pad. In this section, the finite element model, the contact and friction laws are presented. Then, the loading conditions used to model the braking force are detailed. Finally, the boundary element model which allows us to calculate noise emissions is presented.

### 2.1 Finite element model and contact/friction formulation

As previously explained, the focus is on a simplified brake system which is composed of a disc and a pad. These two components are modelled with simplified geometries and both are circular (see Figure 1 (a)). The inner radius of the disc is clamped and the outline of the upper surface of the pad can only translate along the normal direction. These boundary conditions are widely used in this kind of investigation and they are close to the configuration of a real brake system. The finite element model contains about 34000 degrees of freedom and eight-node linear hexahedron elements are used. A convergence study of the finite element mesh has been performed with respect to the finite element length and it shows that the model is valid up to 15 kHz (result not presented). However, this convergence study has been performed for the non coupled system (i.e. without contact/friction). The material and geometrical properties used are listed in Table 1 and the geometrical parameters are illustrated in Figure 1 (b).

The friction interface between the disc and the pad is modelled by introducing nine uniformly spaced contact elements as shown in Figure 1 (b). The contact force is described with a cubic law in order to fit experimental pad compression curves and contact/loss of contact configurations is taken into account [20]. Thus, the disc and the pad can separate at several local nodes of the friction interface. The contact force vector for a given node can be written as shown in

**Table 1**

Material and geometrical properties of the brake system

<b>Material properties</b>			<b>Disc</b>	<b>Pad</b>
Young's modulus	$E$	GPa	125	2
Density	$\rho$	kg.m <sup>-3</sup>	7200	2500
Poisson's ratio	$\nu$		0.3	0.1
Inner radius	$R_{\text{inner}}$	cm	3.4	9.1
Outer radius	$R_{\text{outer}}$	cm	15.1	14.7
Thickness	$t$	cm	1.9	1.28
Pad angle	$\theta$	degree	-	50
<b>Model parameters</b>				
Linear stiffness	$k_{\text{L}}$	$9e^4$	Nm <sup>-1</sup>	
Cubic stiffness	$k_{\text{NL}}$	$4e^9$	Nm <sup>-3</sup>	
Damping percentage	$\xi$	1	%	
Damping rate	$\zeta_i$	10	-	

Equation 1.

$$F_{\text{contact},z}^{\text{d}} = \begin{cases} k_{\text{L}}\delta + k_{\text{NL}}\delta^3 & \text{if } \delta < 0 \\ 0 & \text{otherwise} \end{cases} \quad (1)$$

where  $\delta = X_{\text{p}} - X_{\text{d}}$  is the relative displacement,  $X_{\text{p}}$  and  $X_{\text{d}}$  denote the normal displacements of the pad and the disc respectively (see Figure 1 (c)).  $k_{\text{L}}$  and  $k_{\text{NL}}$  are the linear and cubic stiffnesses,  $F_{\text{contact},z}^{\text{p}}$  and  $F_{\text{contact},z}^{\text{d}}$  are the components of the normal contact force vector applied to the pad and the disc respectively. It can be noted that  $F_{\text{contact},z}^{\text{p}} = -F_{\text{contact},z}^{\text{d}}$ . Figure 1 (c) illustrates a contact element introduced at the friction interface during contact configurations. The main limitation of this formulation is that it allows penetration between the disc and the pad. However, it is able of reproducing mode-coupling instabilities.

For the frictional definition, we consider a simplified Coulomb law with a constant friction coefficient without stick-slip motion. Thus, the nonlinear friction force vectors over the tangential plane of the friction interface are defined by:

$$\begin{cases} \mathbf{F}_{\text{friction}}^{\text{d}} = \mu F_{\text{contact},z}^{\text{d}} \frac{\mathbf{v}_{\text{r}}}{\|\mathbf{v}_{\text{r}}\|} \\ \mathbf{F}_{\text{friction}}^{\text{p}} = -\mathbf{F}_{\text{friction}}^{\text{d}} \end{cases} \quad (2)$$

where  $\mathbf{F}_{\text{friction}}^{\text{d}}$  and  $\mathbf{F}_{\text{friction}}^{\text{p}}$  are the friction force vectors applied to the disc and the pad respectively.  $\mathbf{v}_{\text{r}}$  is the relative velocity vector between the disc and the pad. In this paper, the rotation velocity of the disc is assumed to be such that the relative velocity direction is constant. This global formulation for the finite element model with the contact assumption does not attempt to capture all effects realistically. However, this modelling has been chosen to illustrate a suitable range of behaviour and to investigate the nonlinear behaviour and acoustic emission of the system subjected to various time dependent ramp loadings. For the interested reader and more details on this point, Butlin et al. [7] and Hetzler [21] highlight the fact that a sliding velocity dependent friction coefficient is much more realistic than a constant one. On the other hand, in the present formulation, the linear and cubic stiffnesses are constant: this allows a non-physical penetration between the disc and the pad. To avoid this phenomenon, a penalty algorithm which adjusts the contact stiffnesses can be used to apply an impenetrability

condition. More details about the importance of the contact law in squeal initiation can be found in [5].

The structural mesh convergence, has been investigated for the non-coupled system (i.e. without contact/friction): the contact elements are uniformly spaced over the interface mesh; therefore, their positions change with the mesh refinement and the coupled model convergence cannot be observed. The coupled system modes are very sensitive to the interface mesh refinement and for the reader comprehension, it can be mentioned that this inaccuracy/limitation in modelling can influence the numerical results and the conclusions of the present study.

## 2.2 Loading conditions

During the braking process, a hydraulic pressure is applied to the back-plate of pad. The brake slows down the rotation of the wheel by the friction caused by pressing the pad against the disc. So, during braking, time dependent pressure forces are transmitted from the piston to the pad, compressing the rotating disc. In most studies, the loading conditions are a constant pressure (i.e. the transient dynamic behaviour is undertaken around the sliding equilibrium point [15]). As the focus is only on the disc and the pad, the vibrations of the surrounding are neglected. However, the vibrations of the calliper can result in a time dependent normal loading applied over the pad. Therefore, for a more realistic brake simulation, forced vibrations play a role together with self-excitations.

In this paper, attention is paid to the influence of the pressure forces, transmitted from the piston to the pad, on the nonlinear dynamic behaviour of the brake system. To carry out this study, three kinds of loading conditions will be tested. The first one considers a static load and the two others are ramp loadings defined by two different speeds of loadings. Equation 3 presents the expression of the ramp loading denoted by  $\mathbf{F}(t)$ .

$$\mathbf{F}(t) = \begin{cases} \frac{t}{t_R} \mathbf{F}_{\max} & \text{if } t \leq t_R \\ \mathbf{F}_{\max} & \text{otherwise} \end{cases} \quad (3)$$

where  $t_R$  is the duration of the linear part of  $\mathbf{F}(t)$ ,  $t$  is the time and  $\mathbf{F}_{\max}$  is the force vector associated with the maximum braking pressure  $P_{\max}$ . The influence of the speed of loading over the brake response is investigated by using different values for the parameter  $t_R$ :  $10^{-1}$  and  $10^{-3}$  second which represent slow and fast loadings respectively. The brake responses for the two previous ramp loadings will be compared with the response of the static load in section 3.2.2.

For the reader comprehension, the integration scheme will be performed around the sliding equilibrium point for the static load: initial condition corresponds to a disturbance around the sliding equilibrium point, whereas a disturbance around zero position (i.e. starting point of the brake) is used for the two ramp loadings.

## 2.3 Equation of motion

Then, the Craig and Bampton method is applied to reduce the brake system size. The reduction basis is composed of all the attachment modes and the first hundred eigenmodes of the structure assuming the interface nodes are held fixed. This reduction provides a good correlation between the whole and the reduced brake models until 20 kHz. This frequency corresponds to the maximum audible frequency so it allows to perform squeal noise calculations in the audible domain. Finally, the equations of motion for the reduced model are given by Equation 4:

$$\mathbf{M}\ddot{\mathbf{X}} + \mathbf{C}\dot{\mathbf{X}} + \mathbf{K}\mathbf{X} = \mathbf{F}_{\text{NL}}(\mathbf{X}) + \mathbf{F}(t) \quad (4)$$

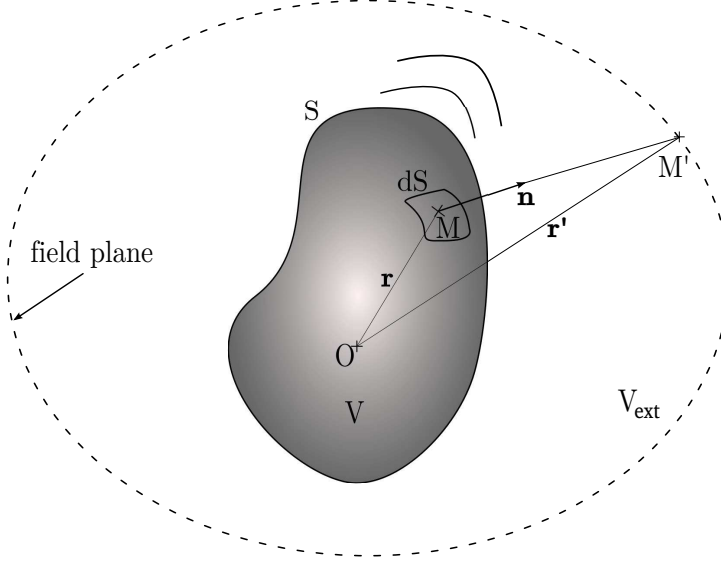


**Fig. 2.** Illustration of the Kirchhoff-Helmholtz integral

where  $\mathbf{M}$ ,  $\mathbf{C}$  and  $\mathbf{K}$  are mass, damping and stiffness matrices.  $\mathbf{X}$  is the generalized displacement vector and the dot denotes derivative with respect to the time.  $\mathbf{F}_{\text{NL}}$  defines the global nonlinear force vector which contains linear and nonlinear parts of the contact force vector and also the friction force vector for both disc and pad. Involving the damping matrix  $\mathbf{C}$ , the following modal damping is applied: a damping percentage  $\xi$  is applied for stable modes and a damping rate  $\zeta_i$  is used for unstable modes, where  $i$  denotes the indice of an unstable mode. The damping and contact parameters used in this analysis are listed in Table 1.

## 2.4 Boundary element method

In this part the focus is on the calculation of the sound pressure radiated by the disc brake subjected to friction-induced nonlinear vibrations. The sound pressure is given by the Fredholm integral equation of the second kind (see Equation 5 and Figure 2):

$$\alpha P(\mathbf{r}') = \int_S \left( P(\mathbf{r}) \frac{dG(\mathbf{r}'|\mathbf{r})}{dn} - G(\mathbf{r}'|\mathbf{r}) \frac{dP(\mathbf{r})}{dn} \right) dS \quad (5)$$

where  $S$  is the surface of the body,  $\mathbf{r}$  defines a point over the surface  $S$  (i.e. coordinates of  $M$  in Figure 2),  $\mathbf{r}'$  defines a point over the field plane (i.e. coordinates of  $M'$  in Figure 2). For a surface point ( $M' \in S$ ),  $0 < \alpha < 1$  whereas for a field point ( $M' \in V_{\text{ext}}$ ) the coefficient  $\alpha$  is equal to 1 and in this case, Equation 5 is called the representation formula. The normal vector  $\mathbf{n}$  is directed into the computational domain. The volume  $V_{\text{ext}}$  is the free space and  $G$  is the Green's function for 3-D free space defined by:

$$G(\mathbf{r}'|\mathbf{r}) = \frac{e^{-j n_{\text{wave}} |\mathbf{r} - \mathbf{r}'|}}{|\mathbf{r} - \mathbf{r}'|} \quad (6)$$

where  $j^2 = -1$  and  $n_{\text{wave}}$  denotes the wave number. The boundary element collocation method is used to discretize the surface  $S$  with elements  $S_k$  and the sound pressure is approximated with shape functions such as:

$$P(\mathbf{r}) \approx \sum_{k=1}^{N_{\text{elt}}} \lambda_k \nu_k(\mathbf{r}) \quad (7)$$

where  $N_{\text{elt}}$  denotes the number of elements,  $\nu_k$  are the shape functions and  $\lambda_k$  are the pressure components onto the shape function basis. Therefore, Equation 5 takes the following form:

$$\alpha \mathbf{P} = \mathbf{A} \mathbf{P}_S - \mathbf{B} \frac{d\mathbf{P}_S}{dn} \quad (8)$$

where the vector  $\mathbf{P}_S$  corresponds to the sound pressure over the boundary element mesh  $S$ , and the vector  $\mathbf{P}$  is the sound pressure in  $V_{\text{ext}}$ . The field of normal velocity over  $S$  is known in the acoustic problem so that  $\frac{\partial \mathbf{P}_S}{\partial n}$  is known. The coefficients of the matrices  $\mathbf{B}$  and  $\mathbf{A}$  are composed of integrals of the Green's function  $G$  and correspond to the BEM matrices. Finally, the BEM equation is given by:

$$\alpha \mathbf{P} = \mathbf{A} \mathbf{P}_S + jcn_{\text{wave}}\rho_{\text{air}} \mathbf{B} \mathbf{V}_S \quad (9)$$

where  $n_{\text{wave}}$  is the wave number,  $\rho_{\text{air}}$  is the density of the fluid,  $c$  is the speed of sound and the vector  $\mathbf{V}_S$  denotes the field of normal velocity over the surface  $S$  in the Fourier frequency space. For the numerical acoustic study, parts of the Open BEM toolbox are used [22]. For a theoretical background about the Boundary Element Method, the reader could refer to [23, 24].

## 2.5 Disc brake boundary element mesh and normal velocity treatment

In this work, the surface mesh is built by wrapping the finite element mesh of the disc brake. The boundary element mesh is composed of quadrangular element with linear shape functions. In this work, only the upper part of the previous skin is selected as illustrated in Figures 3 (a) and (b). This approximation is due to the fact that, in our cases, the normal surface velocity of the circumferential disc surface is almost nil. This investigation can be conducted only with the dynamic response calculation which will be detailed in the next section. Therefore, the upper and lower surfaces can be assumed to be disconnected: only the upper surface contributes to the noise radiation along the  $+\mathbf{z}$ -direction. On the other hand, reflections between the disc and the pad also play an important role in the noise radiations.

Considering the friction interface, it can be observed that this surface can radiate only during loss of contact configuration. So, this area is not considered in the acoustic calculation. However, it is important to note that the disc and the pad have separated finite element meshes. So, the nodes located over the outside boundary between the disc and the pad have to be merged during the wrapping process (see Figures 3 (a) and (b)). Merging those nodes highlights the problem of normal velocity field approximation. Actually, as seen on Figure 3 (c), the disc and the pad have different velocities and normals at the connected points. When the connection is performed, an unique normal  $\tilde{\mathbf{n}}$  is built as illustrated in Figure 3 (d). The disc and the pad velocities are then projected onto the new normal. The first approximation used in this paper consists of averaging the normal velocities of the connected points as shown in Figure 3 (d). The second approximation deals with the contact model used. The interior nodes of the interface are not taken into account but the nodes over its boundary are considered (i.e. connected points). As explained in Section 2.1, the contact formulation allows for penetration between the disc and the pad, and the previous connected points can experience penetration. During this kind of configuration, these nodes are not in contact with the fluid and so cannot radiate. In this study, this phenomenon is neglected and these nodes velocities are considered in the acoustic problem.

On the other hand, there are some limitations with this approach. The first one involved the fact that the finite element mesh and the boundary element mesh have been matched together. This method is not the most accurate and a wrapping mesh algorithm could be used to optimize the surface mesh and to avoid integrations errors. For the reader comprehension, an extensive study of the structural mesh with a wrapping mesh algorithm has been previously performed by Oberst et al. [19] and the authors show that this point plays a significant role in the acoustic

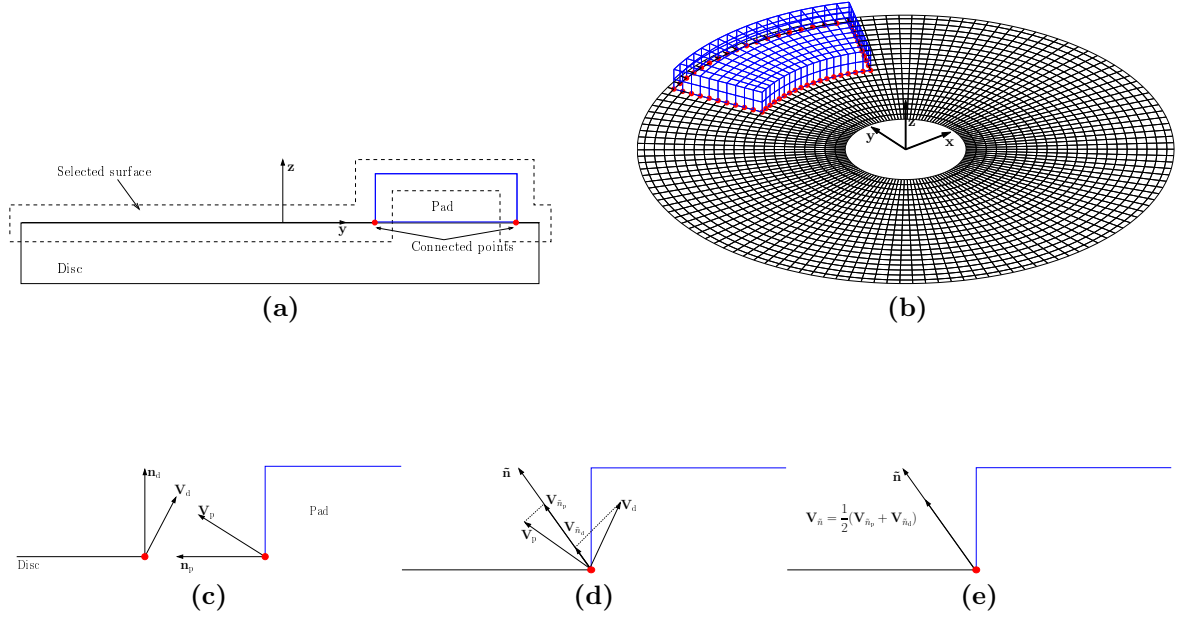


**Fig. 3.** Building of the boundary element mesh and normal velocity treatment. (a): illustration of the surface mesh selection; (b): boundary element mesh; (c): disconnected meshes (finite element mesh); (d): meshes connexion process; (e): averaging velocities on the connected points (final boundary element mesh)

response accuracy. A common rule to determine the mesh characteristic length is to use from 6 to 10 elements per wavelength [25].

In order to build the BEM mesh, the characteristic length has been determined to reach the convergence of the surface sound pressure associated with the highest frequency under study (about 20 kHz). It is observed that a characteristic length of about  $8 \times 10^{-3}$  m is fine enough to reasonably well describe the radiations associated with this frequency.

Another important point involving the use of the BEM is the appearance of characteristic frequencies. These frequencies correspond to the eigenfrequencies of the corresponding interior problem: they have no physical meaning and are only mathematical singularities. To estimate the validity of the BEM mesh, a unit surface velocity is applied, the sound pressure level is calculated at a field point and for the frequency range under study. Then, the curve of the level against the frequency is analyzed to detect irregular peaks which correspond to the irregular frequencies. In our case, the BEM model does not present irregular frequencies in the frequency range [0 20] kHz. Several numerical methods are efficient to avoid these singularities and the interested reader could refer to [26, 27].

### 3 Numerical simulation of brake squeal

The study of friction-induced vibrations for brake systems can be divided into three parts: the stability analysis, the generation of nonlinear vibrations, and the estimation of the sound pressure. In the following sections, these three approaches will be detailed and the list of cases investigated in this work is presented.

### 3.1 Stability analysis

In order to predict the occurrences of squeal nonlinear vibrations, a classical stability analysis can be performed.

For a dynamic system, instabilities are defined by the divergence of a quasi-static sliding equilibrium configuration due to friction. The sliding equilibrium configuration  $\mathbf{X}_0$  is defined by Equation 10:

$$\mathbf{K}\mathbf{X}_0 = \mathbf{F}_{\text{NL}}(X_0) + \mathbf{F}_{\text{max}} \quad (10)$$

which corresponds to the nonlinear static problem associated with the maximum hydraulic pressure applied  $P_{\text{max}}$ . Then, the dynamic system is linearized around the static sliding equilibrium configuration and the stability is given by performing a complex eigenvalue analysis of the linearized system for a given set of parameters (contact, damping, material and geometrical properties). The complex eigenvalue analysis of the linearized system is given in Equation 11:

$$\left( \lambda^2 \mathbf{M} + \lambda \mathbf{C} + (\mathbf{K} - \mathbf{J}_{\text{NL}, \mathbf{X}_0}) \right) \Phi = \mathbf{0} \quad (11)$$

where  $\lambda$  and  $\Phi$  are the eigenvalues and eigenvectors matrices respectively.  $\mathbf{J}_{\text{NL}}$  corresponds to the linearized expression of the nonlinear force vector  $\mathbf{F}_{\text{NL}}$  around  $\mathbf{X}_0$  (Equation 12).

$$\mathbf{J}_{\text{NL}, \mathbf{X}_0} \tilde{\mathbf{X}} = \sum_i \left. \frac{\partial \mathbf{F}_{\text{NL}}(\tilde{\mathbf{X}})}{\partial \tilde{\mathbf{X}}_i} \right|_{\mathbf{X}_0} \tilde{\mathbf{X}}_i \quad (12)$$

where  $\tilde{\mathbf{X}}$  is the disturbance of the equilibrium point  $\mathbf{X}_0$ . The complex eigenvalues provide information about the local stability of the sliding equilibrium point. If all eigenvalues have negative real parts,  $\mathbf{X}_0$  is a stable configuration. If at least one eigenvalue has a positive real part,  $\mathbf{X}_0$  is an unstable equilibrium point which can lead to nonlinear oscillations. Finally, the stability of the nonlinear system is the same as the linear one and this result is provided by the Lyapunov theorem.

For  $P_{\text{max}} = 12.5 \times 10^5$  Pa and  $\mu \in [0; 1]$ , the system presents two classical cases of instabilities: one and two unstable modes (see Figure 4). The first instability is detected for  $\mu = 0.72$  and the associated fundamental frequency  $f_1$  is 929.8 Hz as illustrated in Figure 4 (a). The second instability occurs for  $\mu = 0.731$  and the fundamental frequency  $f_2$  is 9421 Hz (Figure 4 (b)). In the following next section (i.e. analysis of the nonlinear vibration and calculation of noise), we will focus on three cases: a configuration without unstable equilibrium point ( $\mu = 0.69$ ), a single instability case ( $\mu = 0.72$ ) and a case with two unstable modes ( $\mu = 0.731$ ). The stability results are listed in Table 2.

It is important to note that the previous stability analysis and the calculation of the sliding equilibrium point are performed with a static load  $\mathbf{F}_{\text{max}}$ .

**Table 2**

Stability results: material properties, contact and damping parameters of Table 1,  $P_{\text{max}} = 12.5 \times 10^5$  Pa and  $\mu \in [0, 1]$ .

Case	Friction coefficient	Frequency $f_1$ (Hz)	Frequency $f_2$ (Hz)	Area of stability
1	0.69	-	-	stable
2	0.72	929.8	-	one unstable mode
3	0.731	930	9420.9	two unstable modes

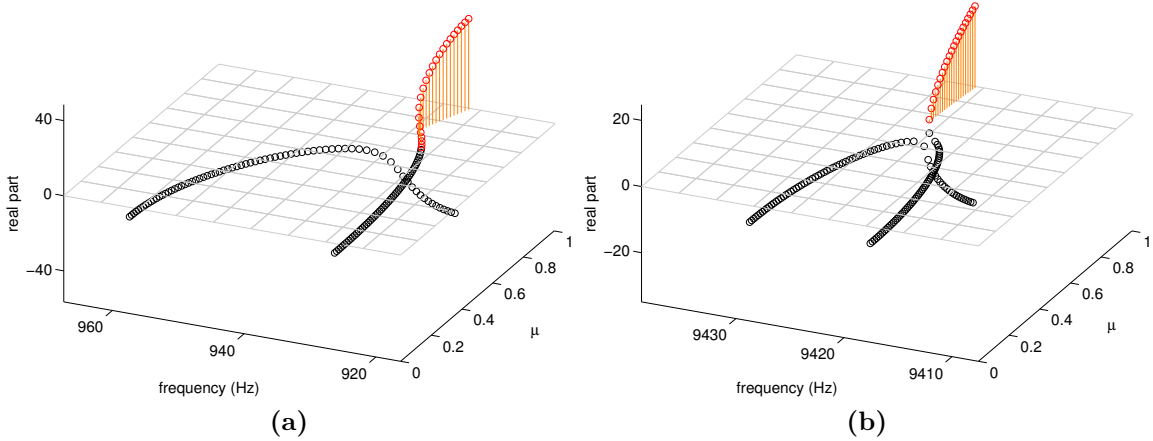


**Fig. 4.** Stability analysis of the brake system, real part against frequency and friction coefficient. (a): first instability; (b): second instability

### 3.2 Nonlinear vibrations

As explained in [15,28], the stability may lead to an under-estimation or over-estimation of the unstable modes observed in the nonlinear time simulation due to the fact that linear conditions are not valid during transient oscillations. Moreover, applying an time dependent braking pressure can influence the generation of friction-induced nonlinear vibrations. Therefore, a numerical resolution of the complete nonlinear system with the time dependent applied pressure (see Equation (4)) is performed to estimate the nonlinear behaviour of the transient and stationary responses of the system.

Section 3.1 provides three cases which correspond to three different kinds of stabilities (see Figure 4) and for each cases, two kinds of loading conditions will be investigated: one static load and two ramp loadings. In a first time, the two set of loading and initial conditions used are presented. Then, time responses for all cases are presented and compared.

#### 3.2.1 Loading and initial conditions

The first set of conditions corresponds to time integration initialized with the static sliding equilibrium configuration with a disturbance around this sliding equilibrium point and the loading condition is a static load defined by  $\mathbf{F}_{\max}$ . Most works in the literature uses this approach and the stability analysis defined in Section 3.1 is able to predict occurrences of nonlinear vibrations. The main disadvantage of this approach is the fact that the evolutions of the nonlinear vibrations generated by a temporal loading are neglected. So, the second kind of initial and loading conditions consists of initializing temporal integration with a ramp loading. These two loading conditions are of the forms presented in Equations 13 and 14:

$$\text{Static loading: } \mathbf{F}(t) = \mathbf{F}_{\max}, \mathbf{X}(t=0) = \mathbf{X}_0 + \boldsymbol{\epsilon}, \dot{\mathbf{X}}(t=0) = \mathbf{0} \quad (13)$$

$$\text{Ramp loading: } \mathbf{F}(t), \mathbf{X}(t=0) = \mathbf{0}, \dot{\mathbf{X}}(t=0) = \mathbf{0} \quad (14)$$

where the vector  $\boldsymbol{\epsilon}$  defines a slight disturbance around the sliding equilibrium point  $\mathbf{X}_0$ . For the static load, the numerical simulation will be performed around the sliding equilibrium point due to the fact that this equilibrium verifies Equation 10. For the two ramp loadings, simulations

will be conducted at the start of braking to investigate the influence of the time dependent brake pressure. It can be noted that no disturbance is introduced for the ramp loading case.

**Table 3**

List of cases with static loadings and ramp loadings (Equation 14)

Ramp loading cases		$t_R$ (s)		Static load cases	Friction coefficients
-	$1_{\text{fast ramp}}$	-	$10^{-3}$	$1_{\text{static}}$	0.69
$2_{\text{slow ramp}}$	$2_{\text{fast ramp}}$	$10^{-1}$	$10^{-3}$	$2_{\text{static}}$	0.72
$3_{\text{slow ramp}}$	$3_{\text{fast ramp}}$	$10^{-1}$	$10^{-3}$	$3_{\text{static}}$	0.731

As previously explained, the main objective is to be able to compare the effect of the ramp loadings for both the non-linear vibrations and the acoustic emissions. So, the stability analysis is investigated to be able to compare the different initial conditions regarding the ramp loading (without or with the ramp loading). For the interested reader, it can be observed that the brake system without ramp loading corresponds to a purely self-excited system (i.e. an autonomous system with a static applied load) whereas the brake system with a ramp loading is subjected to the effect of the time dependent ramp. However, for each case, the friction-induced nonlinear vibrations are generated by an unstable point.

### 3.2.2 Time responses and spectrum analysis

#### Destabilization due to the fast ramp loading: case $1_{\text{static}}$ against case $1_{\text{fast ramp}}$

In this paragraph the time responses of cases  $1_{\text{static}}$  and  $1_{\text{fast ramp}}$  are presented. These cases correspond to a friction coefficient of  $\mu = 0.69$  and the stability analysis predicts a stable sliding equilibrium for the case  $1_{\text{static}}$  according to Figure 4 (a).

By using the loading and initial conditions presented in Equation 13, friction-induced nonlinear vibrations cannot be generated. For the reader comprehension, the time integrations are performed for the case  $1_{\text{static}}$  and the amplitudes of the brake vibrations decrease until the sliding equilibrium configuration is reached.

In the case  $1_{\text{fast ramp}}$ , the loading and initial conditions applied are those defined by Equation 14 and the ramp loading used is defined by  $t_R = 10^{-3}$  s. Figure 5 (a) shows the velocity of the case  $1_{\text{fast ramp}}$  for a normal dof of the friction interface. It can be noted the divergence of the velocity during a short transient with high amplitude, and then a stationary regime. Thus, for a fast ramp loading, the system can be subjected to friction-induced nonlinear vibrations which are not predicted by the stability analysis. In order to identify the frequency content of the nonlinear vibrations, spectrum analysis are performed for the case  $1_{\text{fast ramp}}$ . Figure 5 (b) shows the Fourier transform of the velocity and it can be seen that all the resonance peaks are of the form  $\pm m f_1 \pm n f_2$ , where  $f_1$  and  $f_2$  are the fundamental unstable frequencies and  $m$  and  $n$  are positive integers. These linear combinations of the fundamental frequencies correspond to the spectrum of a case presenting several unstable modes. The response is mainly led by  $f_1$  and its harmonics  $2f_1$  and  $3f_1$ . The second fundamental frequency  $f_2$  appears but its contribution is limited. The previous spectrum analysis provides  $f_1 = 944$  Hz and  $f_2 = 9401$  Hz. These frequencies do not correspond to the results given by the stability analysis (see Table 2) but they are close to the frequencies predicted for  $\mu = 0.731$ . The variation of these frequencies can be explained by the evolution of the average position of the brake and the non linearities [15]. In this case, the mean position during the braking process does not reach the associated sliding equilibrium configuration (Figure 7) that has been calculated in section 3.1.

This analysis highlights the fact that the time dependent loading plays a significant role in squeal initiation in addition to nonlinear effects.

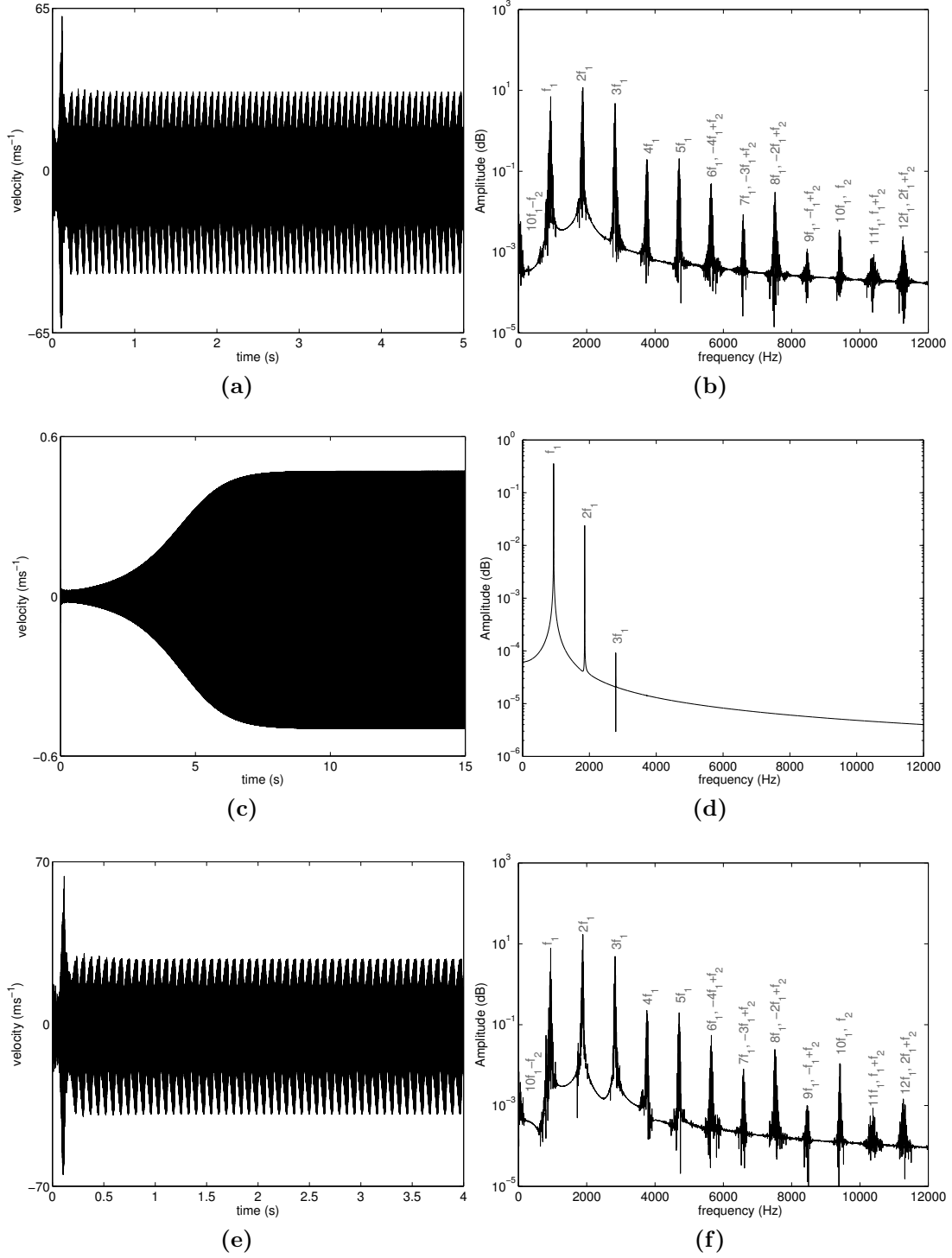


**Fig. 5.** Dynamic responses of cases  $1_{\text{fast ramp}}$ ,  $2_{\text{static}}$  and  $2_{\text{fast ramp}}$ . Column 1: velocity; Column 2: Fourier transform; (a) (b): case  $1_{\text{fast ramp}}$  ; (c) (d): case  $2_{\text{static}}$ ; (e) (f): case  $2_{\text{fast ramp}}$

**Influence of the ramp loading for the single instability cases: case  $2_{\text{static}}$  against cases  $2_{\text{slow ramp}}$  and  $2_{\text{fast ramp}}$**  The time response of the case  $2_{\text{static}}$  is calculated with the static loading and the initial conditions defined by Equation 13. The system leaves the initial

condition and self-excited vibrations are generated as indicated in Figure 5 (c). The associated nonlinear spectrum is composed of the fundamental frequency  $f_1$  and its harmonic components  $2f_1$  and  $3f_1$  (see Figure 5 (c)). The detected fundamental frequency  $f_1$  is 930 Hz and this value is in accordance with the stability analysis prediction. The evolution of the average position, the system oscillates around its static sliding equilibrium configuration throughout the response (Figure 7).

The time response, the spectrum and the mean position of the case  $2_{\text{slow ramp}}$  are exactly the same as for the case  $2_{\text{static}}$  (results not presented).

In the case  $2_{\text{fast ramp}}$ , the time response is significantly different and Figure 5 (e) shows that the amplitude of velocity reaches  $65 \text{ ms}^{-1}$  during transient and the amplitude growth rate is higher than for the cases  $2_{\text{static}}$  and  $2_{\text{slow ramp}}$ . Moreover, the amplitudes during the transient are higher than during the stationary oscillations. The nonlinear spectrum presents harmonic components of the form  $\pm m f_1 \pm n f_2$  as indicated in Figure 5 (f). The two detected fundamental frequencies are  $f_1 = 944 \text{ Hz}$  and  $f_2 = 9424 \text{ Hz}$ :  $f_1$  is different from the frequency predicted by the stability analysis whereas  $f_2$  is very close to the second fundamental frequency predicted for  $\mu = 0.731$ . As previously detailed, the evolution of  $f_1$  can be explained by the nonlinear contacts and loss of contact interactions, and the fact that the system does not oscillate around its static sliding equilibrium configuration (Figure 7). It can also be seen that this response is very similar with the response of case  $1_{\text{fast ramp}}$ .

**Influence of the ramp loading for the case with two unstable modes: cases  $3_{\text{static}}$  against cases  $3_{\text{slow ramp}}$  and  $3_{\text{fast ramp}}$**  According to Figure 4, this friction coefficient of 0.731 provides two unstable modes at 930 Hz and 9421 Hz for the case  $3_{\text{static}}$ .

In the case  $3_{\text{static}}$ , the system diverges from the initial condition (see Equation 13), then stationary oscillations with amplitude of about  $25 \text{ ms}^{-1}$  are observed as indicated in Figure 6 (a). Figure 6 (b) shows that the harmonic components are still linear combinations of the form  $\pm m f_1 \pm n f_2$ . Several components appears but  $f_1$ ,  $f_2$  and  $2f_1$  are predominant.

In the case  $3_{\text{slow ramp}}$ , the features of velocity and spectrum are similar with the case  $3_{\text{static}}$  but the stationary regime is reached much later (results not presented). For the two previous cases, the detected fundamental frequencies are  $f_2 = 9421 \text{ Hz}$  and  $f_1 = 920 \text{ Hz}$  and the latter is not predicted. This is due to the fact that the mean position leaves the sliding equilibrium and the system oscillates around another constant configuration when the stationary regime is reached (Figure 7).

In the case  $3_{\text{fast ramp}}$ , the nonlinear vibrations are significantly different: the velocity presents a predominant transient and the final stationary regime is quickly reached with amplitude of about  $27 \text{ ms}^{-1}$  (Figure 6 (c)) and this is higher than the two previous cases. Moreover, the spectrum is much complex with numerous harmonic components as indicated in Figure 6 (d) but the stationary response is mainly led by  $f_1$ ,  $2f_1$ ,  $3f_1$ . The associated fundamental frequencies are not predicted and this is still due to an evolution of the mean position in addition to nonlinear effects (Figure 7).

Another case associated with a higher friction coefficient of 0.74 has been investigated (results not presented). For this case, the stability analysis shows two unstable modes. Both the static and the fast ramp loading generates higher amplitude of velocity than all the previous cases. Moreover, and as for the previous cases, the mean position does not reached the sliding equilibrium and is different from the mean positions of cases  $1_{\text{fast ramp}}$ ,  $2_{\text{fast ramp}}$  and  $3_{\text{fast ramp}}$ .

The previous analysis show that the amplitude of velocity can be very high. As explained in [29], the limit cycle amplitudes are very sensitive to the friction coefficient. Moreover contact stiffnesses and damping parameters are also important and the parameters used in this work are not experimentally validated and this explains the high amplitude of velocity, in addition

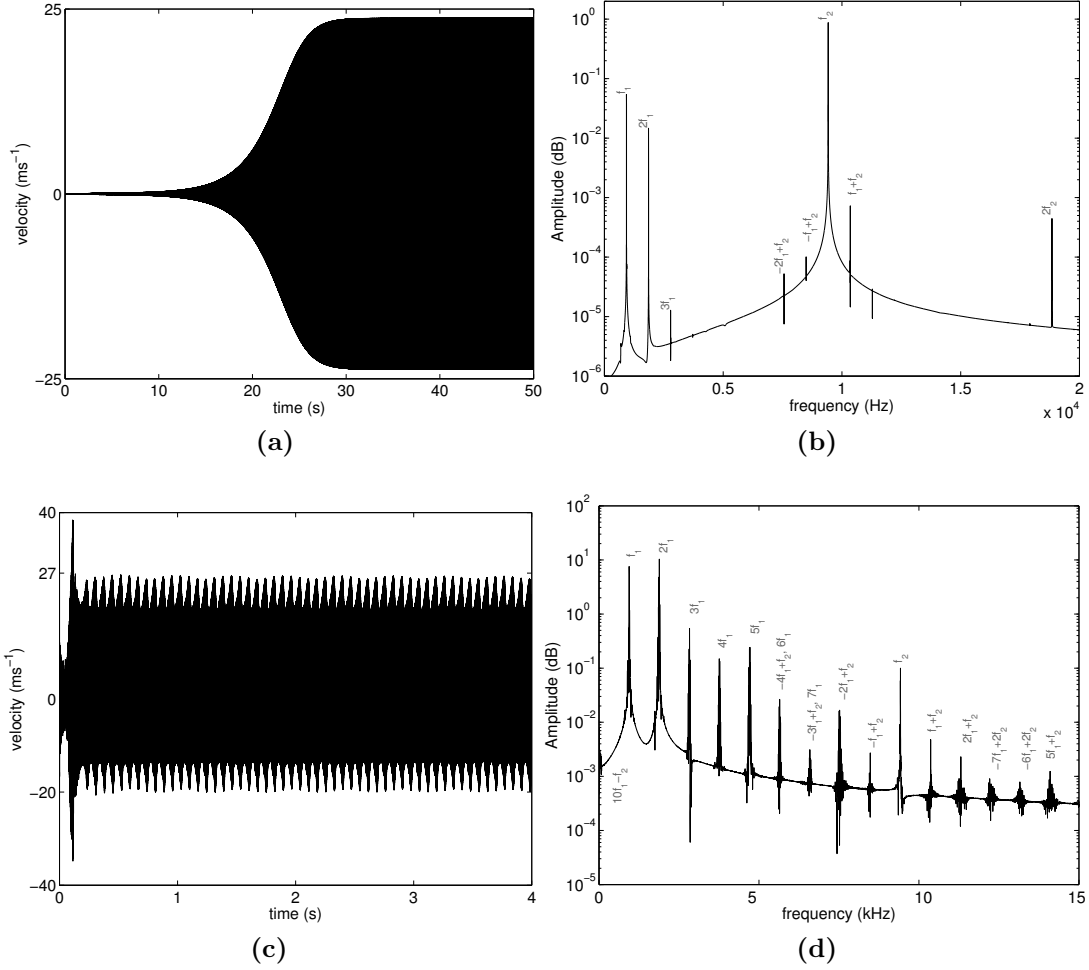


**Fig. 6.** Dynamic responses of cases  $3_{\text{static}}$  and  $3_{\text{fast ramp}}$ . Column 1: velocity; Column 2: Fourier transform; (a) (b): case  $3_{\text{static}}$ ; (c) (d): case  $3_{\text{fast ramp}}$

to the model simplifications.

To conclude this comparison, a “slow” ramp loading provides the same stationary response than a static one whereas a “fast” loading can have several effects. The first corresponds to high amplitude of velocity and is explained by the fact that it generates fast displacement variations which are directly linked to the velocity. The second is the appearance of new harmonic components which are basically associated with cases presenting several fundamental frequencies. This highlights the fact that the ramp loading is able of changing the attractor onto which the system tends to. The final mean positions associated with the cases with a fast ramp loading are close and this explains that the three dynamic responses and spectrum are similar. The last effect is a variation of the fundamental frequencies due to the evolution of the mean position and the nonlinear interactions at the frictional interface.

### 3.3 Noise emissions during squeal event

In this section, attention is paid to the sound pressure field radiated in the free space by the disc brake during squeal event. First of all, the method of calculation which has been developed is remembered and the different field planes over which the sound pressure level is displayed

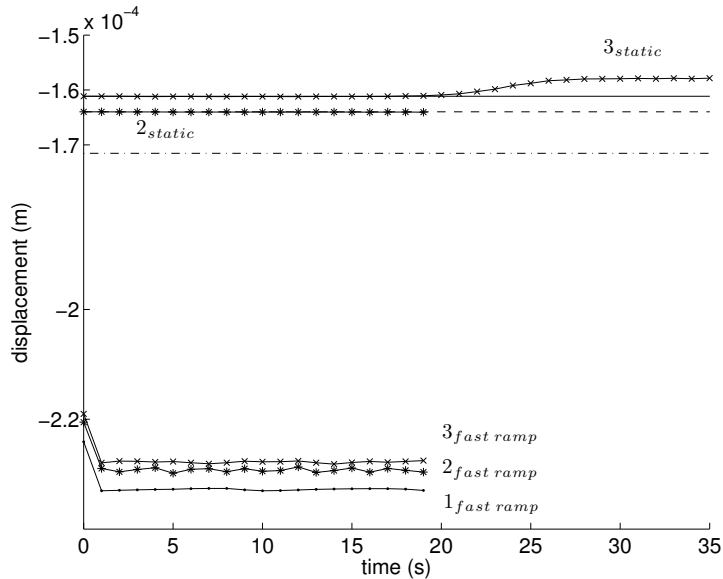


**Fig. 7.** Evolution of the system mean position during the braking process. (—) sliding equilibrium of case 1; (---) sliding equilibrium of case 2; (-·-) sliding equilibrium of case 3; (×) average of cases  $3_{static}$  and  $3_{fast\ ramp}$ ; (\*) average of cases  $2_{static}$  and  $2_{fast\ ramp}$ ; (·) average of case  $1_{fast\ ramp}$

are presented. Then, for all the previous cases (see Table 3), the propagation of squeal noise is characterized in terms of directivity and levels. Finally, a convergence study of the pressure with respect to the number of retained harmonic components is performed.

### 3.3.1 Acoustic calculation method

The multi-frequency acoustic calculation method has been described in [14] but in the current paper, it is reformulated in a more general way. The method of calculation presented in this paragraph aims at calculating the sound pressure generated during squeal phenomenon. This method is based on the resolution of the Fredholm integral equation (see Equation 8) and the main difficulty is that the pressure depends on the frequency of the velocity. However, as previously shown in 3.2.2, the velocity can be composed of several harmonic components due to nonlinear effects. In order to consider this point, the proposed approach can be divided into three steps: the first point of this method is to perform time integration to calculate the field of velocity. The two last steps correspond to the decomposition of the velocity spectrum and the calculation of the sound pressure.

**Detection of the vibration frequencies and decomposition by order:** spectrum analysis are then performed in order to detect all the frequencies which appear in the velocity  $\dot{\mathbf{X}}(t)$ . Resonance peaks are defined by linear combinations of the fundamental frequencies: if the spectrum contains  $p$  fundamental pulsations  $\omega_j$  with  $j \in [1; p]$ , the harmonic components of the response are linear combinations of the following form:

$$k_1 w_1 + k_2 w_2 + \dots + k_i w_i + \dots + k_p w_p \quad (15)$$

with  $k_i \in [-N_h, N_h]$  and  $N_h$  is the number of retained harmonic components. Then, the normal velocity over  $S$   $\dot{\mathbf{X}}_S(t)$  can be decomposed in a Fourier serie which is of the following form:

$$\dot{\mathbf{X}}_S(t) \approx \sum_{k_1=-N_h}^{N_h} \dots \sum_{k_p=-N_h}^{N_h} \mathbf{a}_{k_1, \dots, k_p} \cos(k_1 w_1 + \dots + k_p w_p) t + \mathbf{b}_{k_1, \dots, k_p} \sin(k_1 w_1 + \dots + k_p w_p) t \quad (16)$$

where  $\mathbf{a}_{k_1, \dots, k_p}$  and  $\mathbf{b}_{k_1, \dots, k_p}$  are the Fourier coefficient vectors corresponding to the linear combination of  $w_1, \dots, w_p$ . By introducing the basis  $\boldsymbol{\omega} = [w_1 \dots w_p]^T$  and the vector  $\boldsymbol{\tau} = \boldsymbol{\omega} t$ , the approximated velocity takes the following form:

$$\dot{\mathbf{X}}_S(\boldsymbol{\tau}) \approx \mathbf{a}_0 + \sum_{\mathbf{k} \in \mathbb{Z}^p} \mathbf{a}_{\mathbf{k}} \cos(\mathbf{k} \cdot \boldsymbol{\tau}) + \mathbf{b}_{\mathbf{k}} \sin(\mathbf{k} \cdot \boldsymbol{\tau}) \quad (17)$$

where the vector  $\mathbf{k}$  contains the coefficients of all the linear combination of the fundamental pulsations  $\omega_j$ . It can be noticed that the velocity associated with the harmonic components  $m$  is of the following form:

$$\dot{\mathbf{X}}_{S_m}(\boldsymbol{\tau}) = \mathbf{a}_{\mathbf{k}_m} \cos(\mathbf{k}_m \cdot \boldsymbol{\tau}) + \mathbf{b}_{\mathbf{k}_m} \sin(\mathbf{k}_m \cdot \boldsymbol{\tau}) \quad (18)$$

where  $\dot{\mathbf{X}}_{S_m}$  denotes the contribution of the harmonic components  $m$  in the field of normal velocity over  $S$ . The vector  $\mathbf{k}_m$  corresponds to coefficients of the linear combination of the harmonic components  $m$ . The vector  $\mathbf{a}_{\mathbf{k}_m}$  contains the Fourier coefficients associated with  $\mathbf{k}_m$ .

**Sound pressure radiated and characterization of levels and directivity:** the sound pressure  $\mathbf{P}_{S_m}$  denotes the pressure over  $S$  and corresponds to the harmonic components  $m$ . It depends on the normal velocity field over  $S$  denoted by  $\dot{\mathbf{X}}_{S_m}$ . The boundary element equation (Equation 8) can be solved for each harmonic components: the global wave is decomposed into elementary waves. By using Equation 9, the acoustic equation for the harmonic components  $m$  takes the following form:

$$\alpha \mathbf{P}_m = \mathbf{A}_m \mathbf{P}_{S_m} + j c n_{\text{wave}, m} \rho_{\text{air}} \mathbf{B}_m \mathbf{V}_{S_m} \quad (19)$$

where  $\mathbf{P}_m$  is the sound pressure in the free space and  $n_{\text{wave}, m}$  denotes the wave number associated with the harmonic components  $m$ .  $\mathbf{V}_{S_m}$  is the surface normal velocity in the frequency space associated with the harmonic components  $m$ . It can be noted that the matrices  $\mathbf{A}_m$  and  $\mathbf{B}_m$  depends on the wave number and thus have to be calculated for each harmonic components. A possible way of building the “global” sound pressure is to sum the pressure of each harmonic components  $\mathbf{P}_m$ . However, in the time domain, these components are delayed due to the presence of several fundamental frequencies. To consider these delays, the contribution of  $\mathbf{P}_m$  is weighted by a coefficient corresponding to the ratio between the maximum amplitude of  $\dot{\mathbf{X}}_{S_m}$  and the amplitude associated with an arbitrary time. In this study, the weight associated with  $\mathbf{P}_m$  is denoted by  $\beta_m$  and the associated time step is the one which provides the maximum ratio for the maximum number of components to obtain the maximum sound pressure. Therefore, the reconstructed sound pressure field  $\tilde{\mathbf{P}}$  can be obtained by superposition (see Equation 20):

$$\tilde{\mathbf{P}} = \sum_m \beta_m \mathbf{P}_m \quad (20)$$

Finally, the sound pressure levels in decibels  $L_{\text{dB}}$  are given by  $L_{\text{dB}} = 10 \log_{10} \left( \tilde{\mathbf{P}} \tilde{\mathbf{P}}^* / P_{\text{ref}}^2 \right)$ , where  $P_{\text{ref}}$  denotes the minimum audible sound pressure ( $P_{\text{ref}} = 2 \times 10^{-5}$  Pa), and the star denotes the complex conjugate. In order to characterize the levels in the near and far fields,  $L_{\text{dB}}$  is

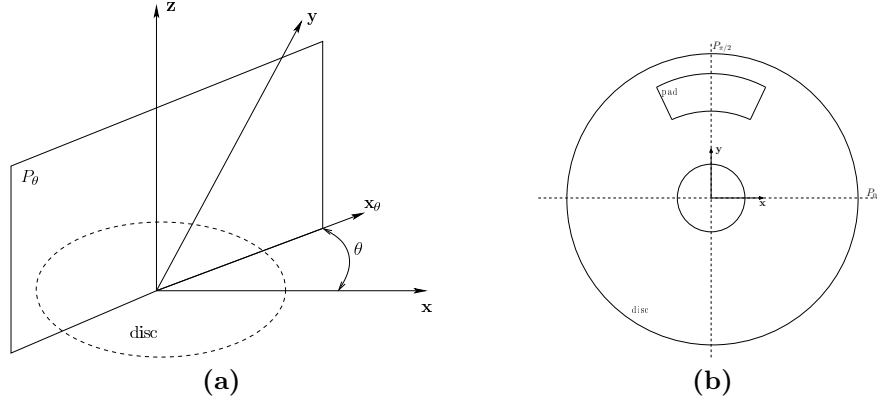


**Fig. 8.** (a) Definition of the field planes  $P_\theta$ ; (b) field planes  $P_\theta$  used:  $P_0$  and  $P_{\frac{\pi}{2}}$

evaluated over five field planes. The first is the boundary element mesh, the second is a square of  $1.5 \times 1.5$  m centered over the disc and placed at  $5 \times 10^{-2}$  m high. The third is a square of  $4 \times 4$  m and placed at 1.5 meter high. Two other planes are also used and correspond to the planes  $P_\theta$  as illustrated in Figure 8 (a). For this study, the values of  $\theta$  will be 0 and  $\frac{\pi}{2}$  (see Figure 8 (b)).

In the following, the term “near field” will denote the field plane placed at  $5 \times 10^{-2}$  m and the term “far field” will be the field plane placed at 1.5 m from the top of the pad. For the interested reader, the precise definition of the near and far fields corresponds to  $n_{\text{wave}}r \ll 1$  and  $n_{\text{wave}}r \gg 1$  respectively, where  $n_{\text{wave}}$  denotes the wave number and  $r$  is the distance between the field point and the source. However, it can be noted that the near field effects do not occur for the previously defined field planes due to the fact that the lower value of  $n_{\text{wave}}r$  is close to 1.

The field plane mesh convergence, i.e. the optimal number of field points which allows us to well describe the sound pressure over a field plane, has been investigated: in our case 1000 field points per plane is fine enough.

### 3.3.2 Calculation of squeal noise

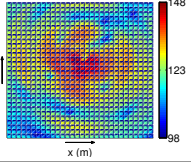
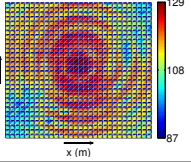
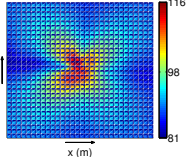
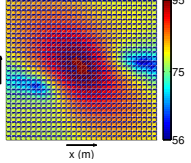
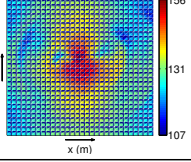
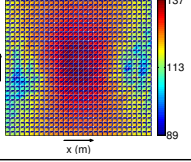
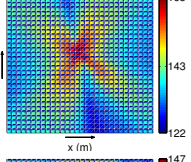
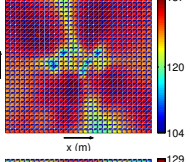
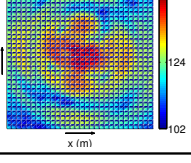
By applying the acoustic calculation method defined in 3.3.1, noise emissions for all the cases during stationary regime are calculated. Attention is paid to the surface velocities and sound pressure levels but also to the radiations over the field planes. Comparisons of the directivity patterns in the near and far fields for all the cases are also presented. An overview of noise emissions in the near and far fields for all the cases is given in Table 4.

**Noise emissions for the case  $1_{\text{fast ramp}}$**  This case corresponds to the destabilization due to the fast ramp loading. An illustration of the surface normal velocity field used for this calculation is presented in Figure 9 (a). This velocity generates a surface sound pressure field with a maximum level of about 166 dB as indicated in Figure 9 (b) and the pad is the most radiating structure in comparison with the disc. Figure 9 (c) shows the 3-D noise propagation and the latter is close to be omnidirectional with the scattering of circular wave front lines which denotes an alternation of low and high sound pressure. The near and far field sound pressure level maps also present a circular propagation of noise (see Table 4).

It can be concluded that destabilization due to the fast ramp loading can generate peculiar

**Table 4**

Comparison of the sound pressure levels in the near and far fields for the cases under study

$\mu$	Case	near field	far field	
0.69	1 <sub>static</sub>	-	-	
	1 <sub>fast ramp</sub>			
0.72	2 <sub>static</sub>			
		2 <sub>fast ramp</sub>		
	0.731	3 <sub>static</sub>		
			3 <sub>fast ramp</sub>	

patterns of noise propagation which are omnidirectional with significant sound pressure levels.

**Noise emissions for the cases 2<sub>static</sub>, 2<sub>slow ramp</sub> and 2<sub>fast ramp</sub>** These cases correspond to the single instability cases defined by a friction coefficient of  $\mu = 0.72$ .

**Case 2<sub>static</sub>:** The surface velocity field of this case presents low amplitude as indicated in Figure 9 (a) and this generates a surface sound pressure with a maximum level of 122 dB (see Figure 9 (b)). The maximum levels are still located over the pad and this repartition generates the 3-D noise propagation of Figure 9 (c). The pattern is smooth due to the contribution of the first fundamental frequency and few of its harmonic components. The directivity presents a predominant central lobe which indicates that the propagation is mainly along the  $\mathbf{z}$ -axis. However, the near field sound presents four predominant lobe whereas only two of them remains in the far field (see Table 4).

**Case 2<sub>slow ramp</sub> :** As explained in Section 3.2.2, time response and spectrum analysis for the case 2<sub>slow ramp</sub> are similar with the case 2<sub>static</sub>. Therefore, acoustic radiations for this case are the same as for the case 2<sub>static</sub> (results not presented). So, the slow progressive load does not disturb both time and acoustic responses.

**Case 2<sub>fast ramp</sub>:** For this case, the normal velocity field shape is different from the two

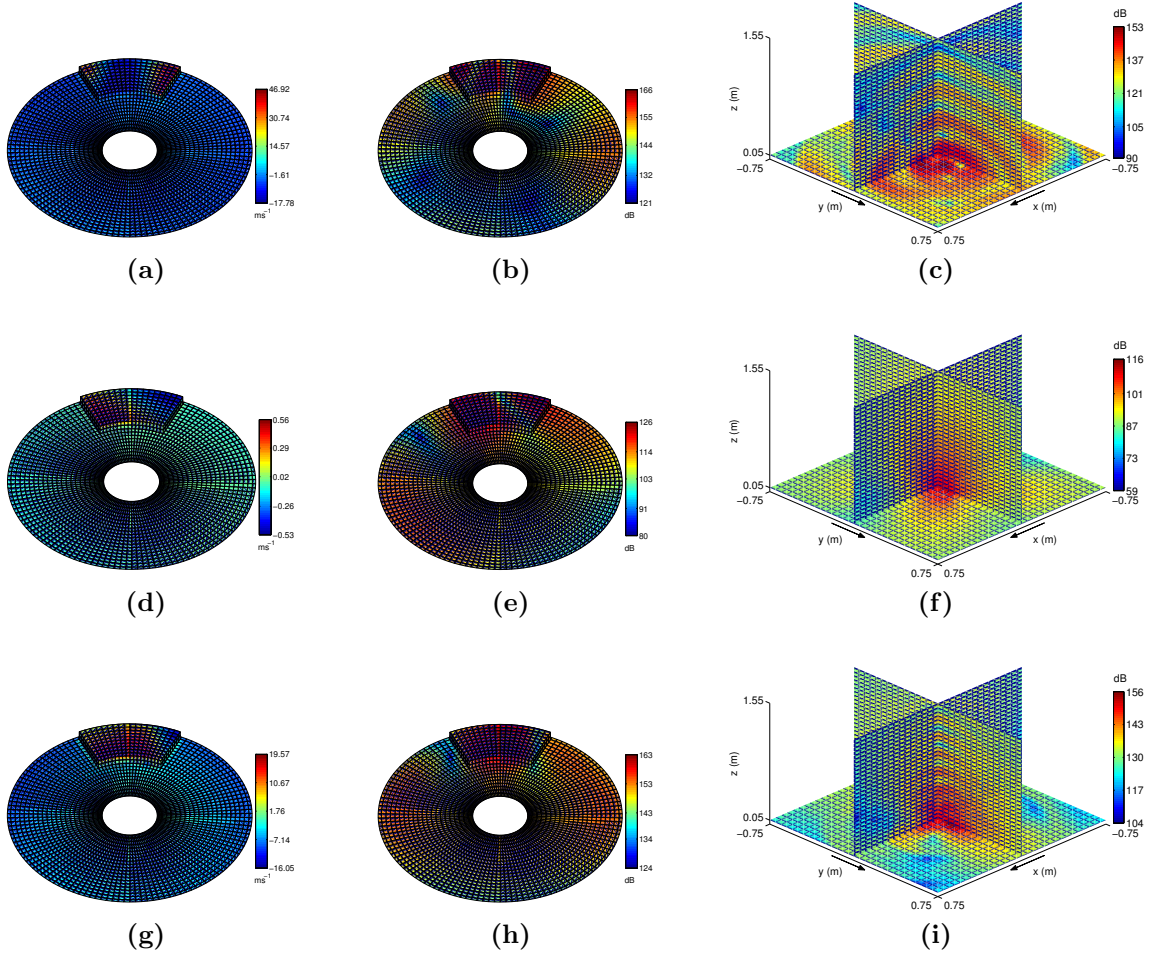


**Fig. 9.** Acoustic responses of cases  $1_{\text{fast ramp}}$ ,  $2_{\text{static}}$  and  $2_{\text{fast ramp}}$  during the stationary regime. column 1: surface normal velocity field; column 2: surface sound pressure level  $L_{\text{dB}}$ ; column 3:  $L_{\text{dB}}$  in the near field  $\cap P_0 \cap P_{\pi/2}$ ; (a) (b) (c): case  $1_{\text{fast ramp}}$ ; (d) (e) (f):  $2_{\text{static}}$ ; (g) (h) (i): case  $2_{\text{fast ramp}}$

previous cases: the amplitudes are higher and the repartition of the maximum amplitudes changes (Figure 9 (g)). This normal velocity field generates a surface sound pressure levels which presents the pattern illustrated in Figure 9 (h) and the maximum level is about 163 dB. Involving the noise propagation, it can be seen on Figure 9 (i) that the pattern seems to be composed of the superposition of a unidirectional propagation (as for the case  $2_{\text{static}}$ ) and circular waves. It has been shown in Section 3.2.2 that the fast ramp loading significantly modifies spectrum: several harmonic components become more predominant than for the static load case. Thus, the previous superposition can be explained by the predominance of  $f_1$  and  $2f_1$  for the case  $2_{\text{fast ramp}}$  in contrast to  $f_1$  for the case  $2_{\text{static}}$ . The near and far field pressures are also modified by this phenomenon (see Table 4).

The acoustic study of cases  $2_{\text{static}}$ ,  $2_{\text{slow ramp}}$  and  $2_{\text{fast ramp}}$  allows to conclude that considering a fast ramp loading can significantly modify squeal noise levels in our cases. Moreover, it completely modifies the directivity patterns due to the predominance and appearance of new harmonic components.

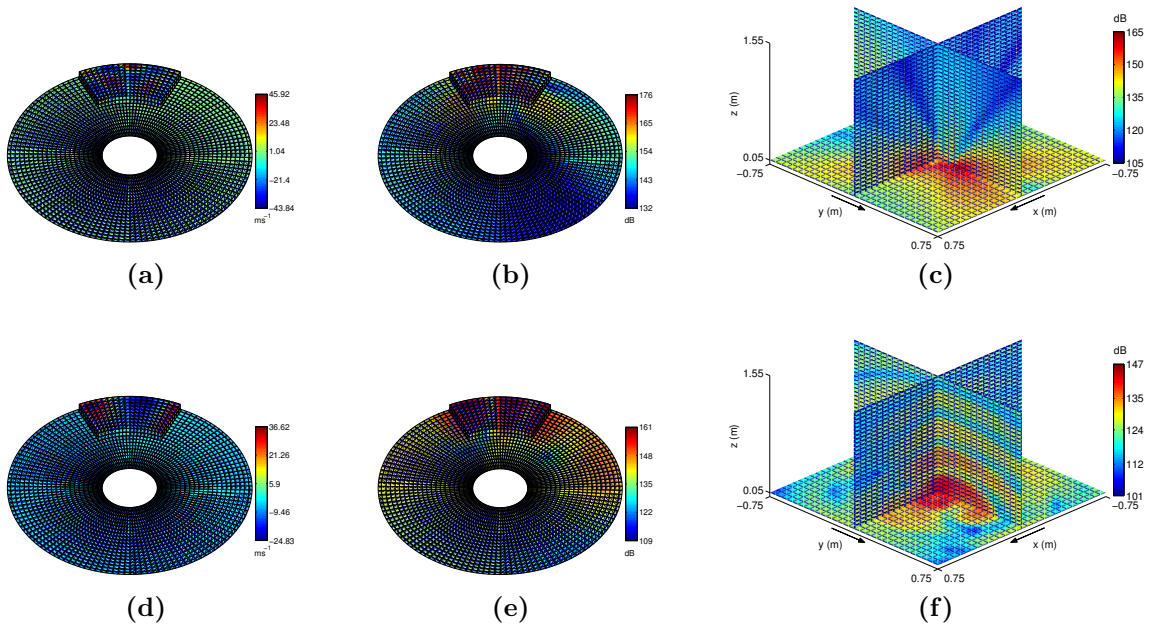


**Fig. 10.** Acoustic responses of cases  $3_{\text{static}}$  and  $3_{\text{fast ramp}}$ . column 1: surface normal velocity field; column 2: surface sound pressure level  $L_{\text{dB}}$ ; column 3:  $L_{\text{dB}}$  in the near field  $\cap P_0 \cap P_{\pi/2}$ ; (a) (b) (c): case  $3_{\text{static}}$ ; (d) (e) (f): case  $3_{\text{fast ramp}}$  during the first stationary regime

**Noise emissions for the cases  $3_{\text{static}}$ ,  $3_{\text{slow ramp}}$  and  $3_{\text{fast ramp}}$**  These cases correspond to the two unstable modes cases with the static load, the slow and fast ramp loadings respectively. For all these cases, noise calculations are performed during the final stationary regime.

**Case  $3_{\text{static}}$ :** In this case, the surface normal velocity field present a complex patter with high amplitude as indicated in 10 (a). Therefore, the surface sound pressure pattern is also complex with several localized maximum over the pad (see Figure 10 (b)). Another point is the fact that acoustic wave reflections of the pad over the disc occur that generate the two lobes over the disc. The maximum level is about 176 dB which is significantly higher than all the previous cases. The 3-D noise propagation is also complex with several lobes which denotes privileged directions of propagation as illustrated in Figure 10 (c). Moreover, the near- and the far- field propagation also present different lobes making the radiations more complex (see Table 4).

**Case  $3_{\text{slow ramp}}$ :** For this case, the acoustic radiations are similar with those of the previous case  $3_{\text{static}}$  (results not presented).

**Case  $3_{\text{fast ramp}}$ :** The surface normal velocity is completely modified in comparison with the two previous cases: the pattern is different and the amplitude is lower as indicates in Figure 10 (d). Therefore, the surface sound pressure levels are also different in terms of patterns and levels (Figure 10 (e)). This surface pressure is very similar to the cases  $1_{\text{fast ramp}}$  and  $2_{\text{fast ramp}}$  and this is explained by the similar spectrum. Finally, for the same reason, the 3-D noise propagation is also similar to the cases  $1_{\text{fast ramp}}$  and  $2_{\text{fast ramp}}$  (Figure 10 (f)).

To conclude this comparison, due to the fact that the “fast” ramp loading strongly modifies the dynamic response, it is able to strongly change the noise radiations. In our cases, the directivity patterns are changed, lobes are changed into circular wave front lines and the levels can be amplified (cases  $3_{\text{static}}$  and  $3_{\text{fast ramp}}$ ) or decreased (cases  $2_{\text{static}}$  and  $2_{\text{fast ramp}}$ ).

This increase/decrease of noise level depends on how the frequency content is modified.

The fast ramp loading tends to increase the normal velocity and the system presents new frequencies which radiates more or less. In our case, the friction coefficient is also able to modify the sound pressure level and the case with a higher friction coefficient of 0.74 (results not presented) presents very high sound pressure level due to high normal velocity for the static load condition. The simplifications in the disc brake modelling are responsible for these unrealistic sound pressure levels. In our cases, the sound pressure levels are higher than the classical squeal noise measurements of about 80-120 dB. However, as the comparison between static and ramp loading cases are performed for the same model, it is relevant to estimate the influence of the loading on the propensity of squeal.

### 3.3.3 Convergence study

As previously explained, all the harmonic components detected in the field of velocity are retained for the acoustic calculations. The calculations are performed for each components and they can be numerous as for the case  $3_{\text{fast ramp}}$ . So, investigating the convergence of the pressure with respect to the number of retained harmonic components can be very use full in terms of time computation. In order to study the convergence, the error  $\epsilon_I$  (see Equation 21) is used :

$$\epsilon_I = \left\| \frac{P_N - P_I}{P_N} \right\| \quad \text{for } i = 1 \dots N \quad (21)$$

where  $I$  denotes the number of retained harmonic components and  $N$  the total number of components.

The relative error for the case  $1_{\text{fast ramp}}$  is presented in Figure 11 (a). It can be noticed that it globally decreases with the number of harmonic components retained. However, several components are more predominant in the convergence than others. By using only  $f_1$  the error is about 5.6% and adding  $f_2$  (i.e using  $f_1$  and  $f_2$ ) does not increase the accuracy. However, adding  $2f_1$  and  $3f_1$  (i.e using  $f_1$ ,  $f_2$ ,  $2f_1$  and  $3f_1$ ) provides an error of 1.4% which is close to the reference (i.e. the sound pressure calculated by retaining all the harmonic components).

Involving the case  $2_{\text{static}}$ , the convergence is fast as illustrated on Figure 11 (b): using  $f_1$  provides an error lower than 0.4% and lower than 0.05% by adding  $2f_1$ . The sound pressure for this case is mainly led by the first harmonic component.

Figure 11 (c) shows the error evolution for the case  $2_{\text{fast ramp}}$  during the stationary regime. The fast ramp loading generates a more complex spectrum with more harmonic components than for the case  $2_{\text{static}}$ . The convergence is slower than for the case  $2_{\text{static}}$  and predominant components are noted. Actually, using  $f_1$  provides an error of about 2% and the components which significantly improve the accuracy are  $2f_1$ ,  $3f_1$ ,  $4f_1$  and  $10f_1 - f_2$  as illustrated in Figure 11 (c).

The error evolutions for the cases  $3_{\text{static}}$ ,  $3_{\text{slow ramp}}$  and  $3_{\text{fast ramp}}$  are not presented, but for the first two, the error is lower than 1% by using only  $f_1$  and  $f_2$ . The cases  $3_{\text{fast ramp}}$  has a different convergence which is similar with the cases  $2_{\text{fast ramp}}$  and  $1_{\text{fast ramp}}$  due to the similarities between the spectrum.

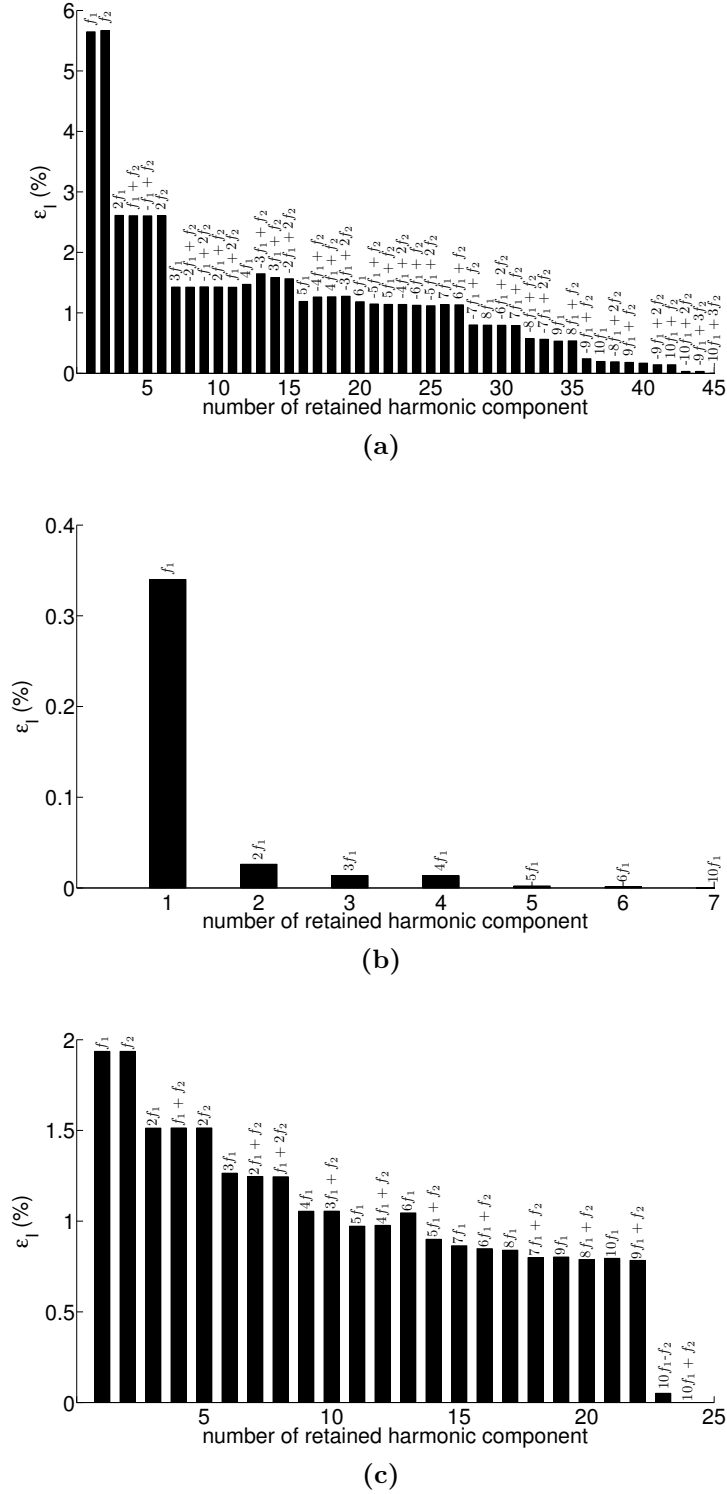


**Fig. 11.** Evolution of the relative error  $\epsilon_I$  with respect to the number of retained harmonic components in the Fourier basis. (a): case  $1_{\text{fast ramp}}$  ; (b): case  $2_{\text{static}}$  during final stationary regime; (c): case  $2_{\text{fast ramp}}$  during final stationary

## 4 Conclusions

This paper focuses on a simplified brake system model composed of a circular disc and a pad. Due non linearities of contact and friction over the interface, the system can be subjected to

friction-induced nonlinear vibrations. The stability analysis of the brake system provides two classical cases of instabilities of one and two unstable modes. For these cases, the time and acoustic responses with the progressive brake pressure are calculated and compared with the static load cases (i.e. purely self-excited vibrations).

Secondly, the numerical results show that a stable configuration predicted by the stability analysis can be destabilized by a sufficiently fast ramp loading. Involving the single and the two unstable modes cases, the ramp loading has three effects: the amplitudes of time response are higher than for the static load; new harmonic components are activated due to non linearities and the fact that the sliding equilibrium configuration is not reached. This investigation highlights the fact that ramp loading can change the attractor onto which the system tends to and thus, strongly modify the brake dynamics.

Thirdly, a method based on the elementary waves superposition which allows us to estimate both levels and directivity of the noise emissions during squeal events has been proposed. A simplified boundary element model of the brake system is used to performed noise calculations. The comparisons of noise emissions between the static and ramp loadings highlight the fact that the directivity pattern is strongly modifies by the time dependent loading due to the modifications of the nonlinear spectrum. Moreover, the levels are also modified: is our cases the fast ramp loading is able of significantly decreasing or increasing the levels.

Finally, the sound pressure convergence study shows that for the static load cases, only the first elementary waves (i.e. associated with the firsts harmonic components) are sufficient to describe the global radiations. However, considering the ramp loading needs more harmonic components to well describe the radiation.

It can be concluded that the friction-induced nonlinear vibrations due to various time dependent ramp loading have a significant influence over the dynamic response in terms of amplitudes and spectrum, and over the acoustic response in terms of noise levels and directivity.

## Acknowledgments

The first author gratefully acknowledges the French Education Ministry which supports this research. The authors thank the financial support provided by the French National Research Agency through the framework of its project ANR-12-JS09-0009.

## References

- [1] N. M. Kinkaid, O. M. O'Reilly, P. Papadopoulos, Automotive disc brake squeal, *Journal of Sound and Vibration* 267 (1) (2003) 105–166.
- [2] S. Oberst, J. C. S. Lai, Chaos in brake squeal noise, *Journal of Sound and Vibration* 330 (2011) 955–975.
- [3] R. A. Ibrahim, Friction-induced vibration, chatter, squeal, and chaos part 1: Mechanics of contact and friction, *American Society of Mechanical Engineers* 47 (7) (1994) 209–226.
- [4] R. A. Ibrahim, Friction-induced vibration, chatter, squeal, and chaos part 2: Dynamics and modeling, *American Society of Mechanical Engineers Applied Mechanics Review* 47 (7) (1994) 227–253.
- [5] H. Hetzler, K. Willner, On the influence of contact tribology on brake squeal, *Tribology International* 46 (2012) 237–246.

- [6] N. Coudeyras, S. Nacivet, J.-J. Sinou, Periodic and quasi-periodic solutions for multi-instabilities involved in brake squeal, *Journal of Sound and Vibration* 328 (4-5) (2009) 520–540.
- [7] T. Butlin, J. Woodhouse, Sensitivity of friction-induced vibration in idealised systems, *Journal of Sound and Vibration* 319 (1-2) (2009) 182–198.
- [8] H. Ouyang, N. Nack, Y. Yuan, F. Chen, Numerical analysis of automotive disc brake squeal: a review, *International Journal of Vehicle Noise and Vibration* 1 (3/4) (2005) 207–231.
- [9] G. Fritz, J.-J. Sinou, J.-M. Duffal, L. Jézéquel, Investigation of the relationship between damping and mode-coupling patterns in case of brake squeal, *Journal of Sound and Vibration* 307 (3-5) (2007) 561–609.
- [10] N. Hoffmann, L. Gaul, Non-conservative beating in sliding friction affected systems: transient amplification of vibrational energy and a technique to determine optimal initial conditions, *Mechanical Systems and Signal Processing* 18 (2004) 611–623.
- [11] F. Massi, L. Baillet, O. Giannini, A. Sestieri, Brake squeal: Linear and nonlinear numerical approaches, *Mechanical Systems and Signal Processing* 21 (6) (2007) 2374–2393.
- [12] F. Chevillot, J.-J. Sinou, N. Hardouin, L. Jezequel, Simulations and experiments of a non-linear aircraft braking system with physical dispersion, *Journal of Vibration and Acoustics* 132 (4) (2010) 041010.
- [13] J.-J. Sinou, A. Loyer, O. Chiello, G. Mogenier, X. Lorang, A global strategy based on experiments and simulations for squeal prediction on industrial railway brakes, *Journal of Sound and Vibration* 332 (20) (2013) 5068–5085.
- [14] K. Soobbarayen, S. Besset, J.-J. Sinou, Noise and vibration for a self-excited mechanical system with friction, *Applied Acoustics* 74 (2013) 1191–1204.
- [15] J.-J. Sinou, Transient non-linear dynamic analysis of automotive disc brake squeal - on the need to consider both stability and non-linear analysis, *Mechanics Research Communications* 37 (1) (2010) 96–105.
- [16] K. Soobbarayen, S. Besset, J.-J. Sinou, Influence of physical parameters and operating conditions for structural integrity of mechanical system subjected to squeal noise, *Key Engineering Materials* 569-570 (2013) 1076–1084.
- [17] U. von Wagner, T. Jearsiripongkul, T. Vomstein, G. Chakraborty, P. Hagedorn, Brake squeal: modeling and experiments, *VDI-Bericht* 1749 (2003) 173–186.
- [18] H. Lee, R. Singh, Determination of sound radiation from a simplified disk-brake rotor by a semi-analytical method, *Noise Control Engineering* 52 (5) (2004) 225–239.
- [19] S. Oberst, J. C. S. Lai, S. Marburg, Guidelines for numerical vibration and acoustic analysis of disc brake squeal using simple models of brake systems, *Journal of Sound and Vibration* 332 (9) (2013) 2284–2299.
- [20] J.-J. Sinou, N. Coudeyras, S. Nacivet, Study of the nonlinear stationary dynamic of single and multi instabilities for disc brake squeal, *International Journal of Vehicle Design* 51 (1-2) (2009) 207–222.

- [21] H. Hetzler, On the effect of nonsmooth coulomb friction on hopf bifurcations in a 1-dof oscillator with self-excitation due to negative damping, *Nonlinear Dynamics* 69 (2012) 601–614.
- [22] V. Cutanda Henriquez, P. Juhl, OpenBEM, <http://www.openbem.dk/>.
- [23] S. Marburg, B. Nolte, *Computational Acoustic of Noise Propagation in Fluids*, Springer.
- [24] M. Bonnet, *Boundary Integral Equation Methods for Solids and Fluids*, John Wiley & Sons Ltd, 1999.
- [25] S. Marburg, S. Schneider, Influence of element types on numeric error for acoustic boundary elements, *Journal of Computational Acoustics* 11 (3) (2003) 363–386.
- [26] H. A. Schenk, Improved integral formulation for acoustic radiation problems, *Journal of the Acoustical Society of America* 44 (1968) 41–58.
- [27] A. J. Burton, G. F. Miller, The application of integral equation methods to the numerical solution of some exterior boundary-value problems, *Proceedings of the Royal Society of London, Series A, Maths Phys Sci* 323 (1553) (1971) 201–210.
- [28] F. Chevillot, J.-J. Sinou, N. Hardouin, Nonlinear transient vibrations and coexistences of multi-instabilities induced by friction in an aircraft braking system, *Journal of Sound and Vibration* 328 (4-5) (2009) 555–574.
- [29] J.-J. Sinou, L. Jézéquel, The influence of damping on the limit cycles for self-exciting mechanism, *Journal of Sound and Vibration* 304 (2007) 875–893.